Tracking of Ice Edges and Ice Floes by Wavelet Analysis of SAR Images

ANTONY K. LIU

Oceans and Ice Branch, NASA/Goddard Space Flight Center, Greenbelt, Maryland

SEELYE MARTIN

University of Washington, School of Oceanography, Seattle, Washington

RONALD KWOK

Jet Propulsion Laboratory, California Institute of Technology, Pasadena, California

(Manuscript received 27 December 1995, in final form 31 January 1997)

ABSTRACT

This paper demonstrates the use of wavelet transforms in the tracking of sequential ice features in the *ERS-1* synthetic aperture radar (SAR) imagery, especially in situations where feature correlation techniques fail to yield reasonable results. Examples include the evolution of the St. Lawrence polynya and summer sea ice change in the Beaufort Sea. For the polynya, the evolution of the region of young ice growth surrounding a polynya can be easily tracked by wavelet analysis due to the large backscatter difference between the young and old ice. Also within the polynya, a 2D fast Fourier transform (FFT) is used to identify the extent of the Langmuir circulation region, which is coincident with the wave-agitated frazil ice growth region, where the sea ice experiences its fastest growth. Therefore, the combination of wavelet and FFT analysis of SAR images provides for the large-scale monitoring of different polynya features. For summer ice, previous work shows that this is the most difficult period for ice trackers due to the lack of features on the sea ice cover. The multiscale wavelet analysis shows that this method delineates the detailed floe shapes during this period, so that between consecutive images, the floe translation and rotation can be estimated.

1. Introduction

Because sea ice serves as an insulator between the ocean and atmosphere, calculation of the heat transfer between the two depends on an accurate determination of floe convergence and divergence, where the divergence generates open water areas within the pack. Specifically, in the pack ice interior and adjacent to coastlines, ice divergence generates quasi-permanent, large openings in the pack called polynyas. Because open water is exposed directly to the atmosphere in polynyas, they are regions of large heat flux and ice growth. This means that the polynyas are also regions of large brine production (Cavalieri and Martin 1994). Given the importance of the polynya heat loss, ice growth, and brine production, we would like to determine the ice divergence rates that generate the polynyas and the resultant polynya areas.

The European *ERS-1* synthetic aperture radar (SAR) data used in this study were received and processed at the Alaska SAR Facility (ASF). In support of ice studies at ASF, the Geophysical Processors System (GPS) has been developed to manipulate and analyze the SAR data as well as provide routine generation of geophysical products. Within the GPS, the ice motion field is generated by first selecting an image pair, then performing an area-based matching predicated on a 2D correlation of the image intensity. This motion tracker has been successful in the Arctic winter (Kwok et al. 1990), but has difficulties with summer ice, coastal polynyas, and the marginal ice zone (MIZ). An alternate tracking method is described by McConnell et al. (1991), who use feature tracking to match floe boundaries in pairs of SAR images. If the ice contrast is reduced so that the boundaries between floes are no longer clear, as occurs in summer, this tracking scheme fails.

Our objective in this paper is to demonstrate the use of a 2D wavelet transform for feature tracking and identification in the SAR imagery, in particular in situations where the feature correlation techniques fail to yield reasonable results. The 2D wavelet transform that we employ is an efficient bandpass filter, which can be used to separate various scale processes and show their relative phase/location information, as shown for SAR im-

Corresponding author address: Antony K. Liu, Oceans and Ice Branch, NASA/Goddard Space Flight Center, Code 971, Greenbelt, MD 20771.
E-mail: liu@neptune.gsfc.nasa.gov

agery by Liu and Peng (1993). The 2D Gaussian wavelet transform (sometimes referred to as the Mexican hat or Laplacian of a Gaussian transform) of an SAR image can be used with a threshold as an edge detector (Canny 1986). In the MIZ study of Liu et al. (1994), the ice edge location in each SAR image has been determined through use of a 2D wavelet transform.

In this paper, we apply the wavelet transform to two examples: the growth of the St. Lawrence polynya in the Bering Sea, and the resolution of the summer ice drift in the Beaufort Sea. Section 2 provides a brief introduction to the 2D Gaussian wavelet. Then, using three consecutive *ERS-1* SAR images of the St. Lawrence Island polynya, section 3 describes the wavelet transform and algorithms used to extract the boundaries of the young ice region, and the wavelet and fast Fourier transform (FFT) methods used to analyze the active polynya region. Section 4 describes the use of the wavelet in floe tracking and applies this work to the St. Lawrence polynya and to summer ice in the Beaufort Sea. Finally, section 5 discusses our results and summarizes our conclusions.

2. Two-dimensional Gaussian wavelet

The wavelet transform $W_s(a, \mathbf{b})$ of a function $s(\mathbf{r})$, where $\mathbf{r} = (x, y)$, is expressed in terms of the complex valued wavelet function $w(\mathbf{r})$ as follows:

$$W_s(a, \mathbf{b}) = \frac{1}{\sqrt{a}} \int s(\mathbf{r}) w^* \left(\frac{\mathbf{r} - \mathbf{b}}{a} \right) d\mathbf{r}, \qquad (1)$$

in which the wavelet function is dilated by a factor, a, and shifted by $\mathbf{b}$. The function $w(\mathbf{r})$ is the basic wavelet that must satisfy the admissibility condition but is otherwise subject to choice within certain limits (Combes et al. 1989). The superscript asterisk indicates a complex conjugate. The mother wavelets frequently used in data analysis are a Gaussian-modulated sine and cosine wave packet (the Morlet wavelet), and the second derivative of a Gaussian (the Mexican hat). In this study, the analyzing wavelet is defined as the second derivative of a Gaussian as follows:

$$w(x, y) = \frac{1}{a} \left(2 - \frac{x^2 + y^2}{a^2} \right) \exp\left(-\frac{x^2 + y^2}{2a^2} \right), \qquad (2)$$

where the standard deviation a is the scale of the wavelet transform. Since convolution is commutative with respect to differentiation, the resulting wavelet transform is the Laplacian of a Gaussian smoothed function. Thus, its zeros correspond to the inflection points of the original function (Canny 1986). The contours of zero crossing indicate the edges in the pattern of the input function. The detailed procedure of wavelet analysis is discussed in the following section.

3. Wavelet analysis for extraction of ice edges from polynyas

a. Algorithms and results

Polynyas are wind-driven regions of thin ice and open water within the pack, which generally form adjacent to coasts. Proceeding away from the coast, a polynya consists of a narrow open water dominated by short wind waves, a region with longer wind waves coincident with the frazil ice organized into the linear Langmuir streaks that are parallel to the wind; an abrupt transition to consolidated young ice, where the width of this region depends on how long the polynya has been open; and finally, another transition to the older pack ice. In the polynya, the largest heat transfer occurs in the wave-agitated region of frazil ice and Langmuir streaks. Within this frazil ice production region, the ocean and ice surface temperature approximately equals the freezing point of seawater, so that the heat transfer is at its maximum (Cavalieri and Martin 1994). We call this the ''active'' polynya region, which has a characteristic downwind length of 1–10 km, dependent on wind speed and temperature. The physical significance of the Langmuir streaks on the images is that their presence implies a region of large heat flux. After the polynya has been open for several days, this active region is surrounded by a region of consolidated thin ice, with downwind lengths of 50–150 km.

This discussion suggests that there are two polynya features that must be identified: the active region of open water and Langmuir streaks, and the consolidated thin ice region downwind of the active region. In SAR images containing floes or polynyas, the boundaries between open water and ice, or young gray ice and older brighter ice, are sometimes easily identified. In such circumstances, a single continuous boundary may be detected through a single-scale wavelet transform by using the Mexican-hat wavelet. The maximum gradient change in pixel intensity along a zero crossing contour determines the boundary location (Liu et al. 1994). Because the pack ice consists of ice floes of multiple scales with complex ice edges, the use of a single-scale wavelet transform may not be applicable.

To overcome the deficiencies of the single-scale wavelet transform, we next describe a more general ice edge algorithm that assembles the ice edge elements from the results of multiscale wavelet transforms. In this algorithm, the method of ''proximity to an approximation'' (Ballard and Brown 1982) developed in the field of computer vision is used to locate a more accurate boundary through use of a distance criteria. A large-scale wavelet transform is used to detect an approximate boundary, then the edge elements from the small wavelet transform are used as boundary points for a more accurate boundary. Several scales can be used to delineate the ice edge as accurately as required. As an example, we next describe the evolution of the St. Lawrence Island polynya.

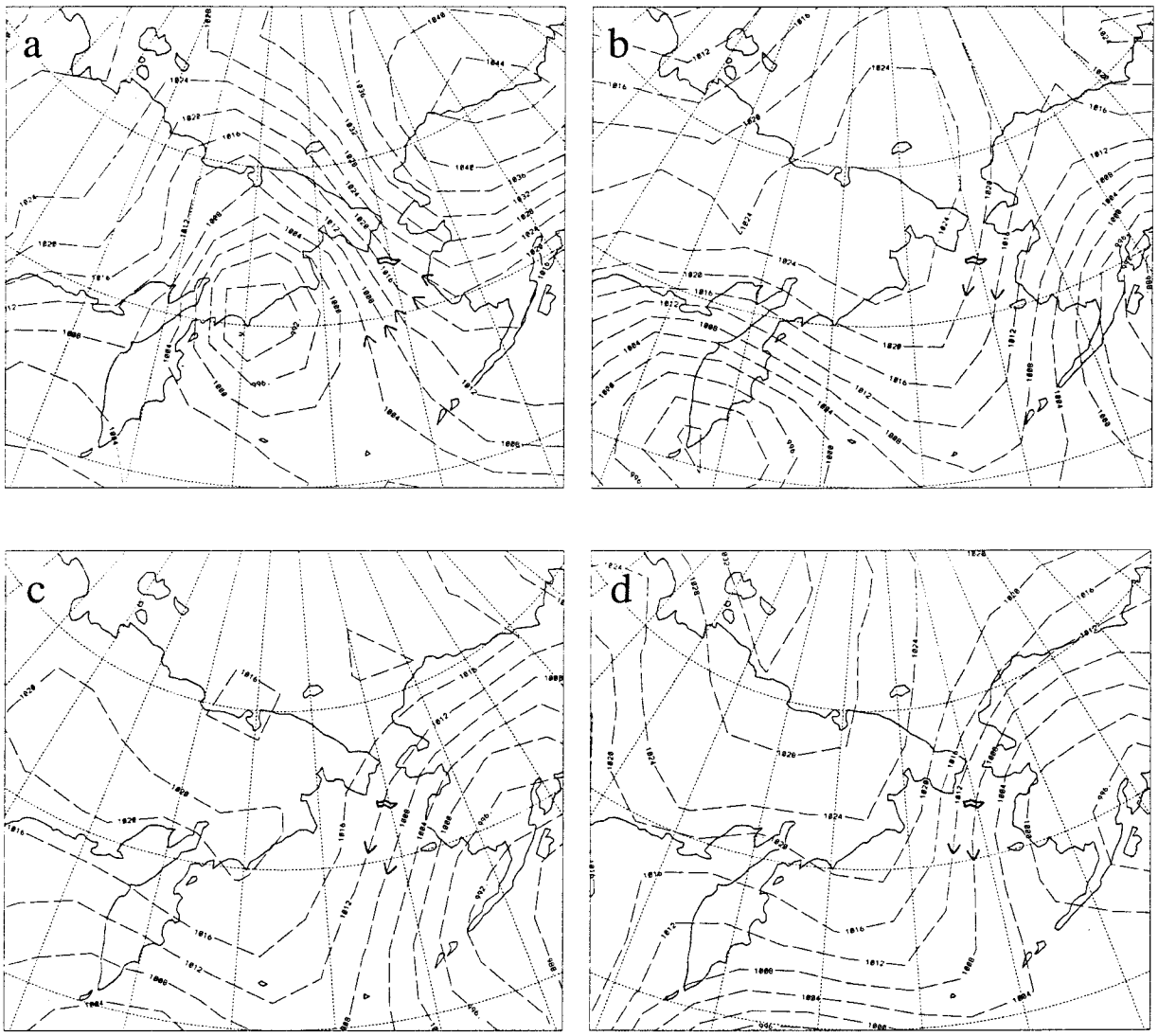

FIG. 1. Surface pressure charts for 1992 in the Bering Sea: (a) 18 February at 1200 UTC, (b) at 0000 UTC 22 February, (c) at 0000 UTC 25, and (d) at 0000 UTC 28 February. On the charts, St. Lawrence Island is outlined in black, and the arrows show the geostrophic wind direction. (Data courtesy of the National Centers for Environmental Prediction.)

This study uses three sequential *ERS-1* SAR images collected over St. Lawrence Island at about 2300 UTC on 21, 24, and 27 February 1992. For this period, Fig. 1 shows four surface pressure charts. The first is from 1200 UTC on 18 February, or four days before the first SAR image; the next three are taken at 0000 UTC on 22, 25, and 28 February so that they are nearly coincident to the SAR images. On these figures, the geostrophic winds are parallel to the isobars and in the direction shown by the arrows. The ice drift is approximately parallel to the geostrophic winds at about 0.8% of the wind speed (Thorndike and Colony 1982). Figure 1a shows that preceding the SAR images, the Bering Sea is dominated by a strong low pressure system, which generates southwesterly winds and drives the pack ice north against the south side of St. Lawrence Island. Figure 1b shows that by 22 February the situation reverses, and the weather is dominated by the Siberian high pressure system, which generates strong northeasterly winds over the island and drives the pack ice away from the coast. The three SAR images show that during this period of strong northeast winds, the polynya grows and spreads to the south.

Although the ice drift responds to the geostrophic winds, at the ocean surface, the heat flux and direction of the Langmuir streaks depend on the 10-m wind speed and direction. For the times of the SAR images, Table 1 lists the 10-m air temperature and the 10-m wind speed and direction, where the air temperatures are derived by optimal interpolation from the surrounding weather stations (E. Munoz 1995, personal communication). The 10-m winds are derived from the geostrophic winds at

TABLE 1. The 10-m air temperature, wind speed, and wind direction as calculated south of St. Lawrence Island, at 0000 UTC vs day in February. The wind direction is given in terms of the direction from which the wind comes.

Date	Air temperature (°C)	Wind speed (m s^{-1})	Direction (°)
22	−19	6.0	62
25	−13	8.4	65
28	−19	11.4	58

a point immediately to the south of the island, using a reduction factor of 0.7 for the wind magnitude, and a rotation to the right of 32° (Overland and Colony 1994). The table shows that for each day, the surface temperature is well below zero, and the wind speed has about the same direction but increases in magnitude throughout the period.

For three different scales, Fig. 2 shows the wavelet transforms of the 100-m resolution image of the St. Lawrence Island polynya for 27 February, where the opening of polynya on the south side of the island is clearly visible. The image measures 1024 pixels wide and 3072 pixels high, where the pixel size is 100 m × 100 m. In Fig. 2a, the dashed line shows the polynya boundary derived using a large-scale wavelet transform (with $a = 128$ units of pixel spacing) in Eq. (1). In this derivation, because of a large wavelet scale, the edge effects of the wavelet transform may cover such significant portion of the domain that it is impossible to extract any meaningful approximate boundary. To minimize this distortion, the image is first extended in the north–south direction by reflection; then is again reflected in the east–west direction to form a new image that is four times the original size. The wavelet transform is then computed for the new extended image, with only one-quarter of the computed domain retained. Because the edge effect is significantly reduced, the approximate ice edge boundary shown in Fig. 2a can be extracted with a 50% threshold.

For the medium-scale boundary shown in Fig. 2a by the solid line, we choose $a = 16$. The edge elements are not obtained directly from the contours of zero crossing of wavelet transform. As mentioned above, because the smoothing effect of the Mexican-hat wavelet is reduced as its scale becomes smaller, the zero crossing associated with noise proliferates in the whole image, so that it becomes difficult to sort out the true boundary even by threshold. For this case, we obtain the edge elements by selection of the wavelet transform values equal to a fraction of the maximum. The closed contours in Fig. 2a correspond to a threshold value of 5%. The figure shows that most of these closed contours are located in the neighborhood of the approximate ice edge given by the dashed line. Because of the fragmented nature of the boundary between the new and the pack ice, a few closed contours may appear elsewhere in the image. These are eliminated by the following method of proximity.

In the method of proximity, the center of mass of the closed contours is first computed as follows:

$$X_c = (x_c, y_c) = \sum_I (x_i, y_i)/N, \tag{3}$$

where (x_i, y_i) are the coordinates and N is the total number of the points of closed boundary. A distance is then calculated from the center of mass (x_c, y_c) to the approximate boundary B derived from the large-scale wavelet transform. If the distance lies within a certain threshold, in this case 100 m, the point (x_c, y_c) is taken as new point of the boundary between the two ice types. Because these medium-scale boundary points are, in general, sparse and well separated, we then delineate the new boundary by successive connection of each center of mass to its nearest neighbor.

Finally, we choose $a = 4$ and compute the small-scale wavelet transform. Through repetition of the same procedure as above, we generate a new boundary by using the previous medium-scale results as the approximate boundary; Fig. 2b shows this result. Because the new boundary points obtained by the small-scale wavelet transform are, in some locations, randomly distributed around the approximate boundary, a moving average (by taking successive average of the coordinates of these points) may be necessary to facilitate the line linking.

Figures 3a–c summarize the ice boundary calculations for the SAR images of 21, 24, and 27 February, respectively. On these figures, the results of large-scale wavelet transform are indicated by dash–dotted lines, medium scale by dashed lines, and small scale by solid lines. Note that because of the small polynya size on 21 February, there are no results from the large-scale wavelet transform. Figure 4 shows the schematic diagram of the evolution of the young ice in the St. Lawrence Island polynya. The young ice area of polynya within each SAR image can be estimated and its growth rate is found to be 2.52 exp(day/3.36).

b. The active polynya region

For the active polynya region on 27 February, Fig. 5 shows the long, linear streaks characteristic of the Langmuir circulation and its 2D FFT. The transformed image in Fig. 5b shows that the Langmuir cells have many scales with one peak at 120 m and another at approximately 230 m.

Figure 6 shows the use of this Fourier and wavelet transform in the estimation of the areas of the active and thin ice regions. From the high-resolution image on 24 February, and because of the irregular wind pattern downwind of the island, the Langmuir streaks only formed near the western end of the island. The active region area can be estimated from the area covered with Langmuir streaks. To derive this area, we divided the

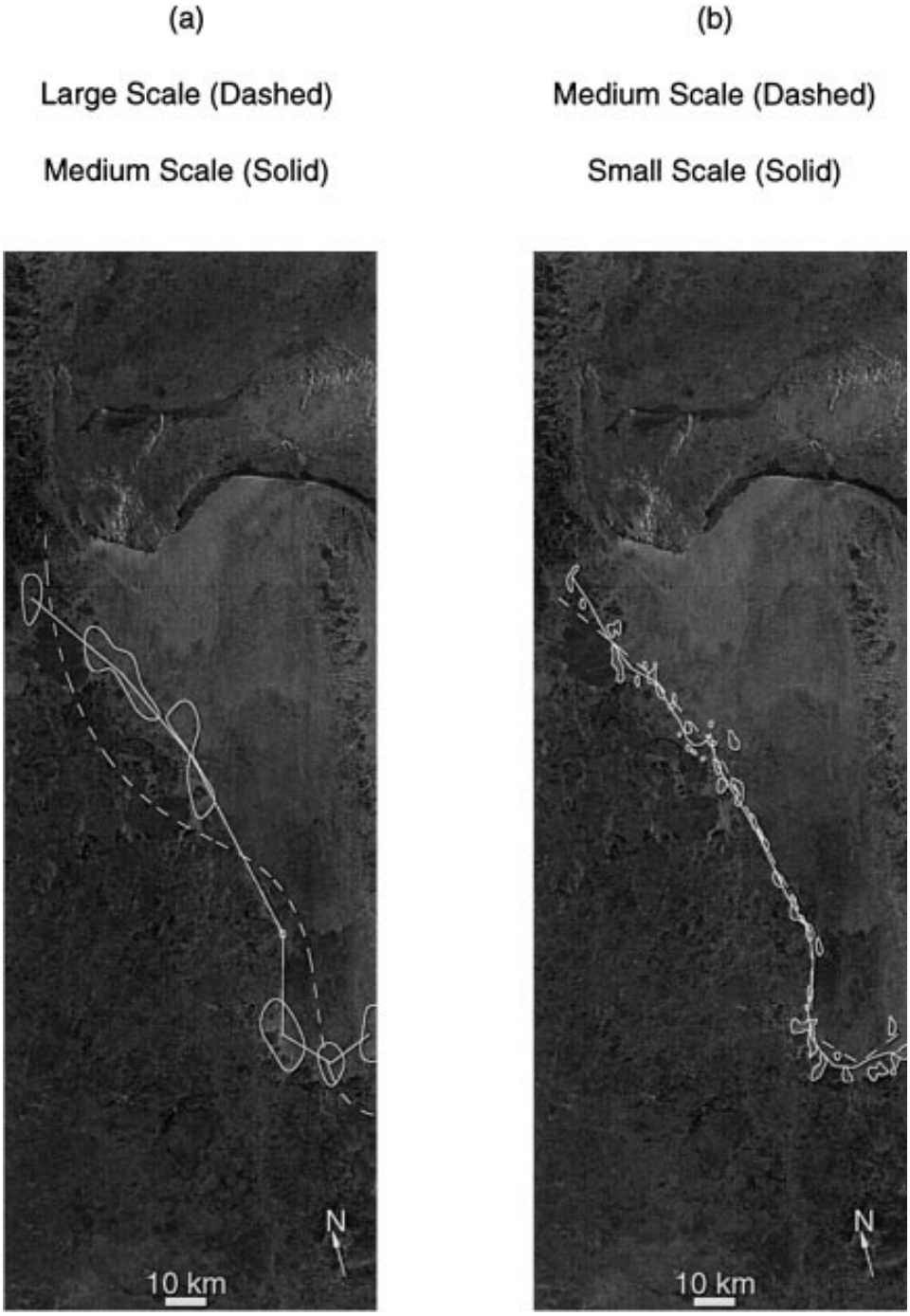

FIG. 2. Wavelet transform of the SAR image for 27 February 1992: (a) large scale (dashed line), and medium scale (solid line), and (b) medium scale (dashed line), and small scale (solid line). The contours are connected by the sliding averages of the center of mass. SAR image copyright ESA 1992.

polynya area into 3 km × 3 km subscenes, then calculated the wave spectra from an FFT for each subscene. The wave spectral density for all waves less than 200 m are then estimated. The area of the active polynya region is determined by a threshold based on the contours of Langmuir cell spectral density as the area covered between the dashed line and the island shown in Fig. 6b. For 27 February, the new ice area is relatively bright in the polynya, which is probably due to Bragg scatter, and it can be directly extracted out with a medium wavelet transform ($a = 16$) inside of the polynya area, as shown in Fig. 6c. For 21 February, the polynya

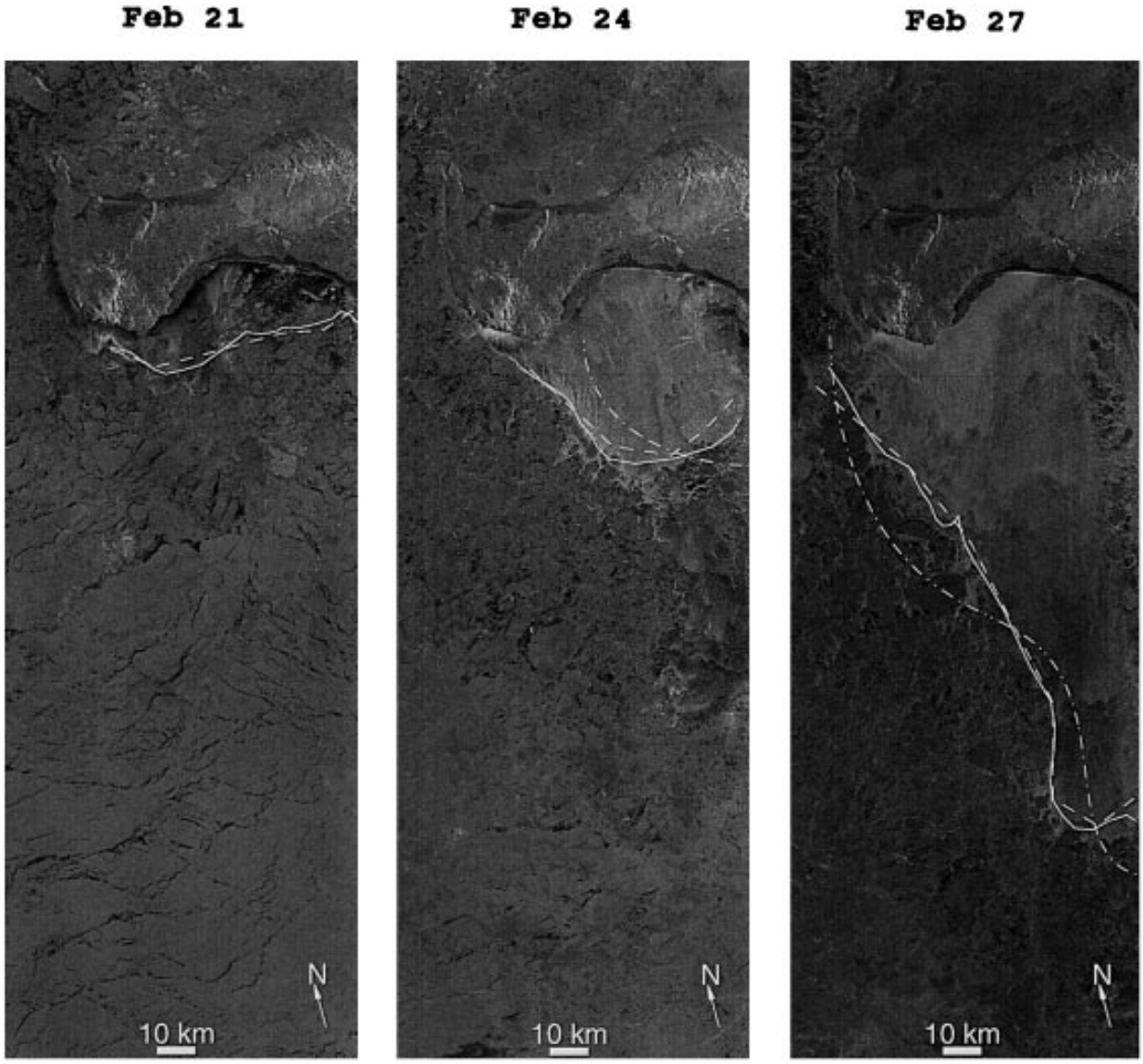

FIG. 3. Summary of the ice edge boundaries derived from the wavelet transforms for (a) 21 February, (b) 24 February, and (c) 27 February 1992. SAR image copyright ESA 1992.

area is relatively small, and a gray scale from the histogram can be used to separate the new ice area (bright) from the young ice area (relatively dark), as shown in Fig. 6a. The evolution of the estimated new ice areas in the polynya (delineated by solid lines) is summarized in Fig. 6 by the dashed lines. The active region, young ice, and consolidated pack ice areas are indicated by I, II, and III, respectively.

4. Wavelet analysis for tracking of ice floes

In the MIZ and the polynyas, because the processes are so dynamic, ice floe tracking at 3-day intervals may be too difficult to achieve on a grid-to-grid basis. Although most of ice floes in these areas may change beyond recognition in a 3-day interval, some large ice floes can still be tracked. We next describe an algorithm for ice floe tracking in these areas, which is based on template matching of the ice floe shapes approximated by closed contours of ice floes obtained from the wavelet transform.

The ice floe tracking procedure is similar to tracking of the ice edge. As an example, we compute the wavelet transform of the St. Lawrence Island SAR images with a scale, $a = 16$, corresponding to a typical ice floe size in this region. Then, we plot the wavelet transform contours with the contour level set at 5% of the maximum. With a nonzero contour level, edge elements corresponding to noisy features are effectively filtered out, and closed contours are generated except near the image

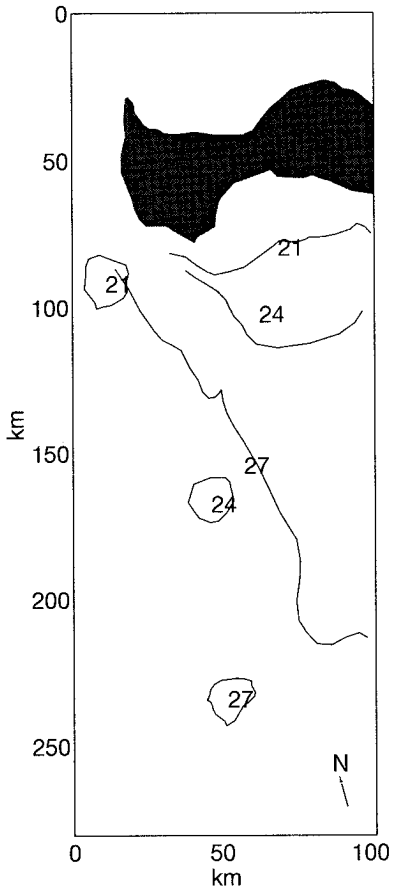

FIG. 4. Schematic diagram of the evolution of St. Lawrence Island polynya for 21, 24, and 27 February. The solid lines show the polynya boundaries, and the closed contours are the ice floe position.

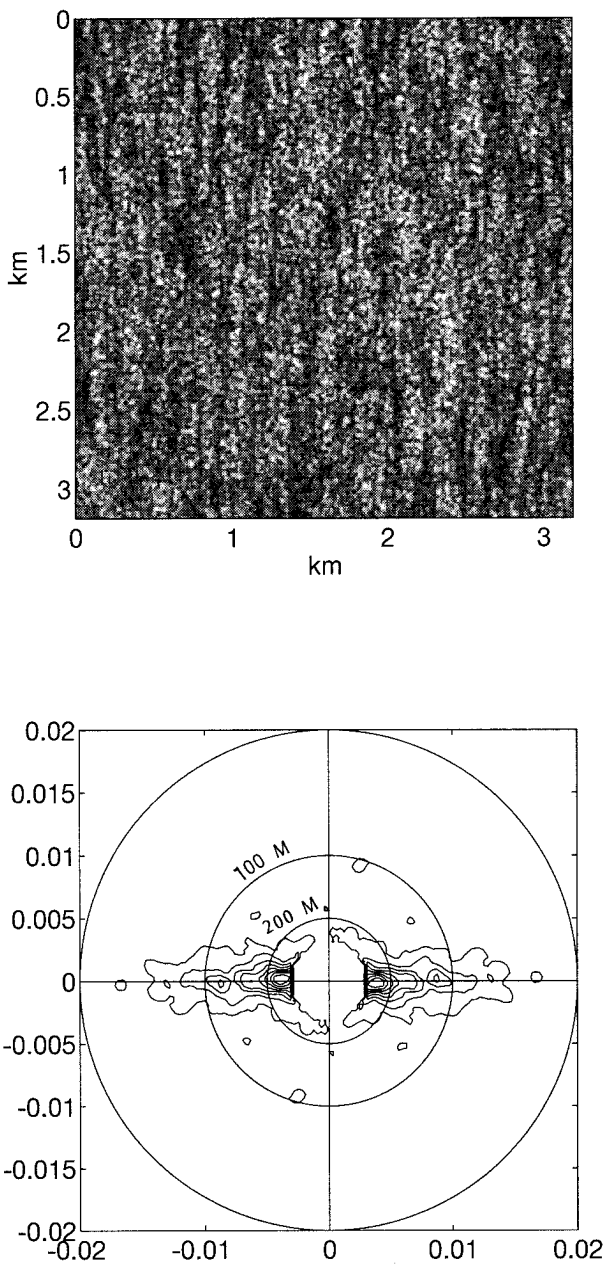

FIG. 5. Analysis of the polynya Langmuir circulation for 27 February. (a) The 25-m resolution image of the circulation, and (b) the FTT spectrum for the Langmuir streaks. In (b), the circular contours lie at 50, 100, and 200 m, respectively. SAR image copyright ESA 1992.

edge. As shown in Figs. 7a and 7b, each closed contour may correspond to the approximate boundary of a large floe or to an area with the same texture. Then, each closed contour is indexed and framed in a rectangular window with its four sides just tangent to the closed contour. For each window, a binary image is generated with pixels within the boundary set to one and those outside the boundary but within the rectangle set to zero. To demonstrate this procedure, we select the prominent floe identified by contour number 16 in Fig. 7a as the initial ice floe.

We then perform template matching on the binary image of the template with each closed contour 3 days later (Fig. 7b). The two binary images are first superimposed at their respective center of mass. For template matching, a metric that measures the degree of mismatch between the template and an unknown pattern is defined as follows (Schalkoff 1992):

$$m = \sum_R |f - g|, \tag{4}$$

where f denotes the template pattern, g is the unknown target pattern, and R is the range of the template pattern f, namely, the window enclosing the closed contour for the template. A small value of m indicates that two patterns are similar; a large value indicates that they are different. Because f and g consist of binary digits, Eq. (4) can be further simplified by

$$m = \sum_R \mathrm{XOR}(f, g). \tag{5}$$

This follows simply from the fact that the method of

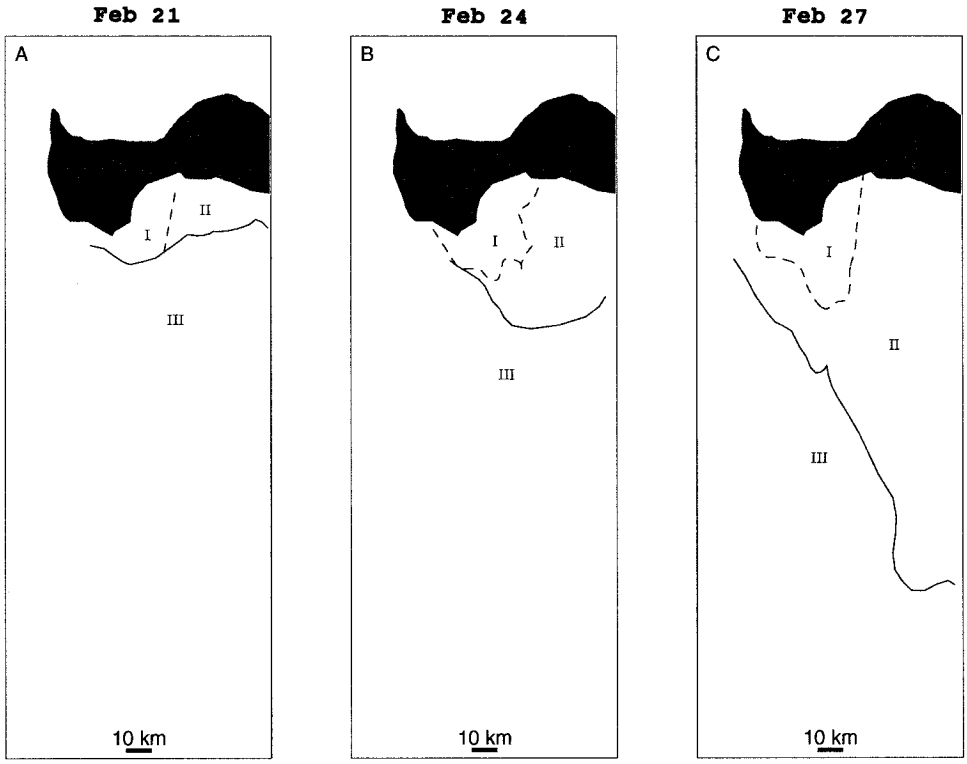

FIG. 6. Ice distribution in the polynya images. The active polynya region is area I, the young ice area is II, and the consolidated pack is III. (a) 21 February, with the new ice area determined by its gray scale; (b) 24 February, with the new ice area estimated by counting Langmuir cells; (c) 27 February, with the area determined with the wavelet transform.

exclusive-or, XOR, of two binary digits always gives 0 when they are of the same value, otherwise 1. Thus, we only need to perform a logical XOR operation on the pairs of pixel values for each closed contour. The pair of binary images with the minimum m are those whose shapes have the best match. Figure 7c shows the sum of the differences m for comparison of all closed contours on 24 February to contour number 16 on 21 February. On 24 February, the contour number 80 has the lowest value of m, and we select it as the matched ice floe. The matched ice floe is then used in turn as a template to be correlated with the ice floes at a later time by repeating the above procedures so that ice floes can be tracked sequentially. Figure 8 shows the summary of our floe tracking results for 21, 24, and 27 February.

After the ice floe has been matched and tracked, a refined boundary can be obtained again by the method of proximity of approximation, discussed above for the ice edge tracking. First, we assemble edge elements obtained by wavelet transform using a small scale ($a = 2$ units of pixel spacing) within the neighborhood of the approximate boundary, and then we link the center of mass of these edge elements consecutively, as shown in Fig. 9. The summary of floe tracking is also shown in Fig. 4. Notice that the detailed shape of the ice floe with sharp edges and corners is well delineated by this method. Based on these detailed floe shapes, the floe translation and rotation can be estimated. The floe speeds are approximately 0.32 m s^{-1} from 21 to 24 February, and then 0.26 m s^{-1} to 27 February. The rotations of floe due to the shear through the opening of polynya are approximately 50° and 40° from 21 to 24 February and to 27 February. Within 6 days, the floe has moved approximately 150 km and rotated about 90°.

In our second case study of ice floe tracking, we use two sequential SAR images in the Beaufort Sea during the summer of 1992 on 23 and 26 August. During summer, there is relatively little contrast between ice types due to the presence of liquid water on top of the ice surface that removes the contribution of the sea ice to the observed backscatter.

Figure 10 shows the contours of wavelet transform of a medium scale ($a = 16$) with an above-zero threshold as a bandpass filter and labeled by index numbers for two SAR images separated by three days. By translation of these two contour maps, the contours from each map are found to match very well, as shown in Fig. 11. Most of contours can be identified after three days, and the degree of change/distortion can be estimated by measuring the difference. The prominent ice floe with lesser change is used to construct its detailed shape using the

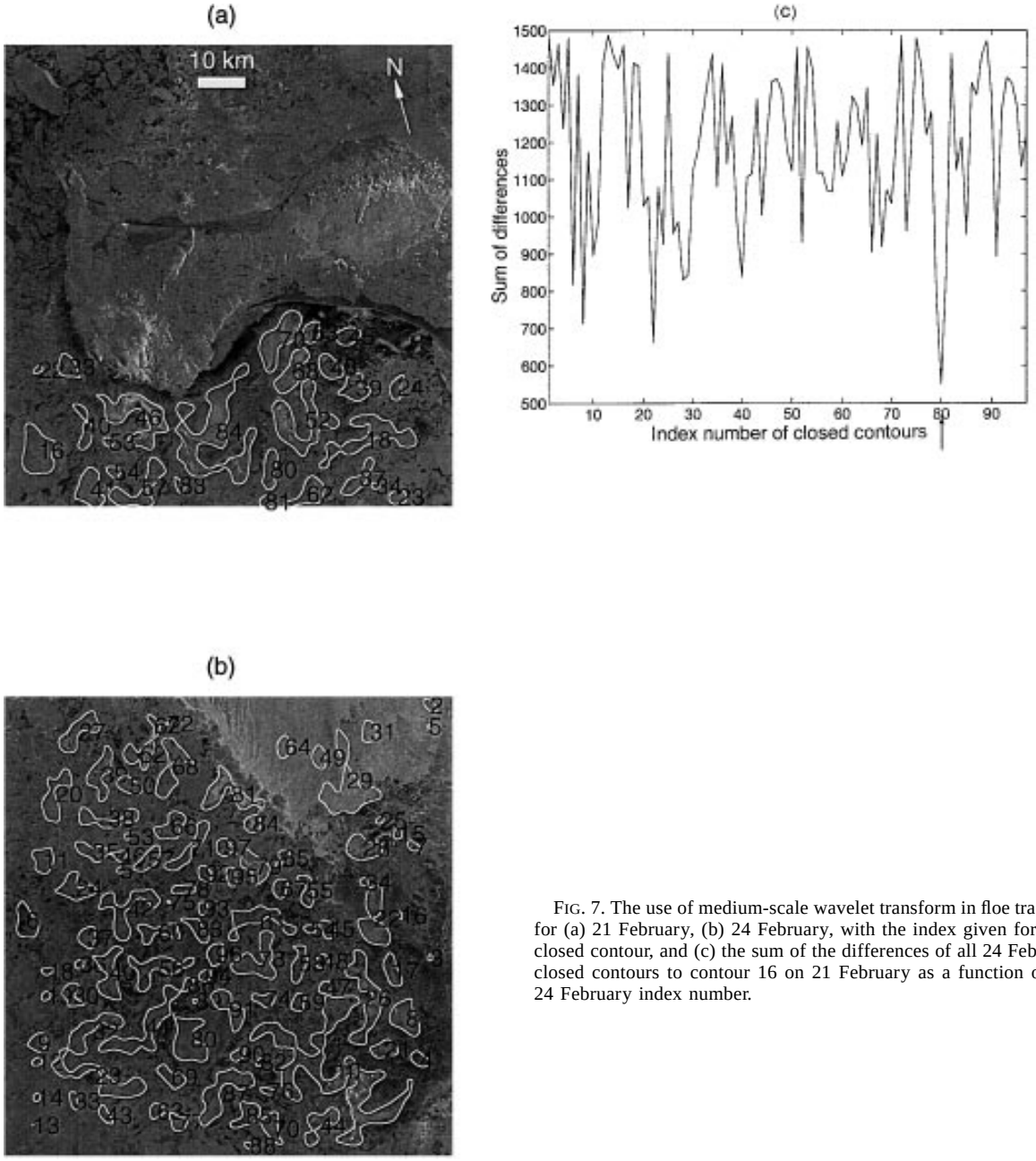

FIG. 7. The use of medium-scale wavelet transform in floe tracking for (a) 21 February, (b) 24 February, with the index given for each closed contour, and (c) the sum of the differences of all 24 February closed contours to contour 16 on 21 February as a function of the 24 February index number.

same method of proximity of approximation. A small scale, $a = 2$, is chosen for wavelet transform to assemble edge elements within the neighborhood of the approximate boundary. The detailed shape of an ice floe can be constructed by linking the center of mass of these edge elements. Figure 12 summarizes the ice floe tracking results and the ice motion vector. Again, based on these detailed floe shapes, the floe motion of both translation and rotation can be estimated. In this case the ice floe speed is approximately 0.12 m s^{-1} with almost no rotation.

5. Discussion

In this paper, the 2D Gaussian wavelet transform is used at several scales to separate texture and features in SAR images of sea ice. The technique is applied to the specific problems of polynya evolution and the determination of the displacement and drift of ice floes in the summer Beaufort Sea. For the specific case of the St. Lawrence Island polynya, our analysis shows that this wavelet procedure can systematically extract geophysically relevant parameters from SAR imagery of

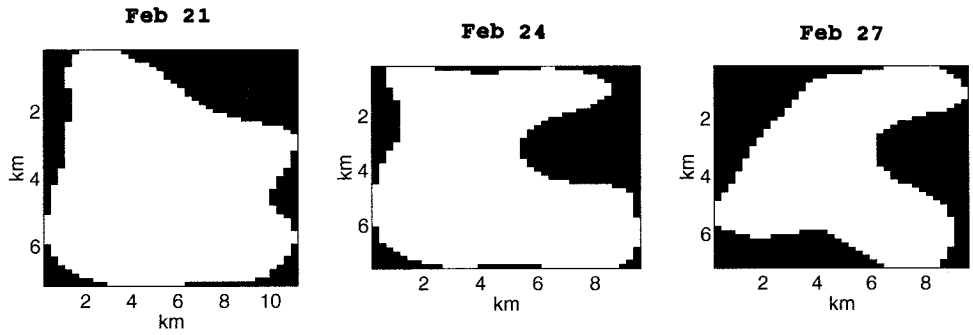

FIG. 8. Summary of the results of the matched floe framed with templates for 21, 24, and 27 February.

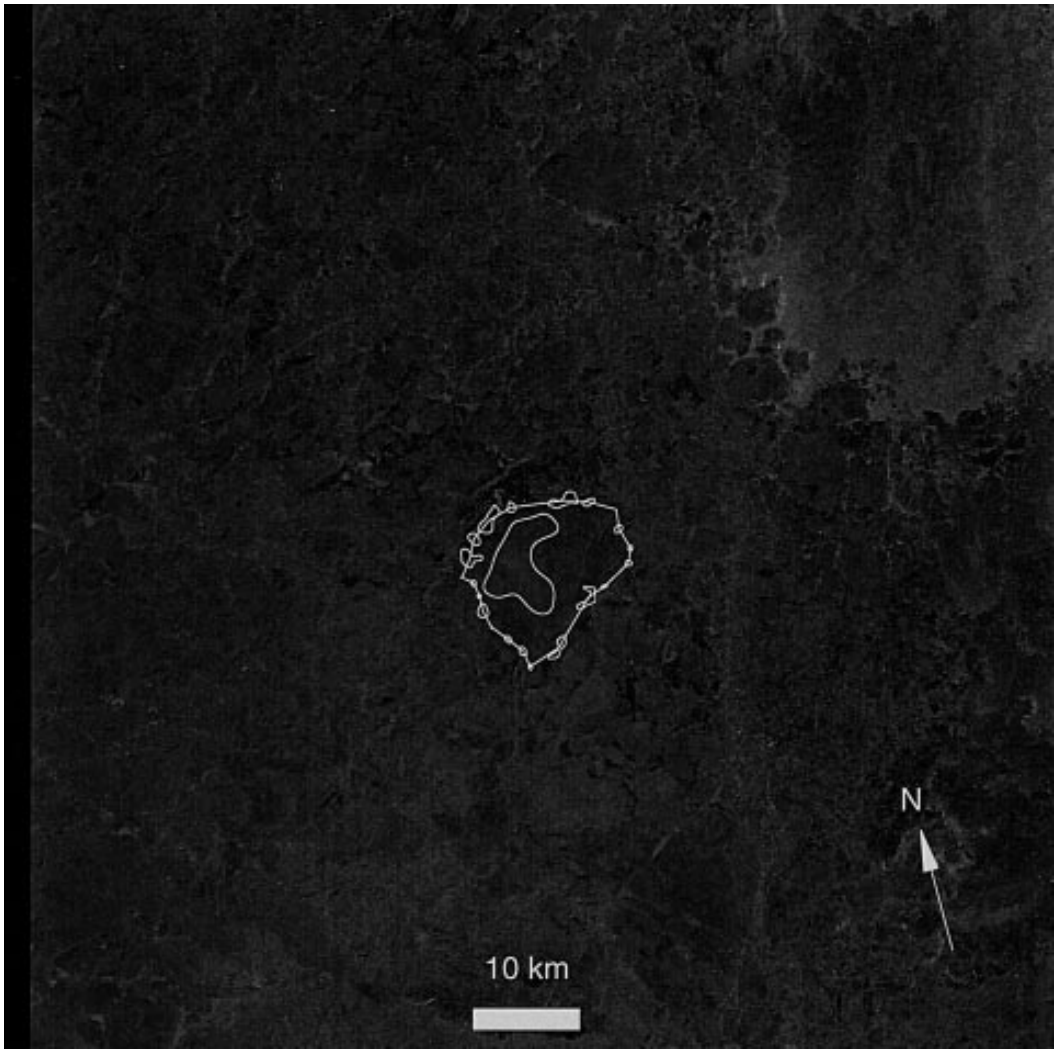

FIG. 9. Floe edge elements (small contours) obtained by wavelet transform using a small scale within the neighborhood of the approximate boundary obtained by wavelet transform with a medium scale. The small contours are connected by the center of mass to construct the detailed shape of ice floe.

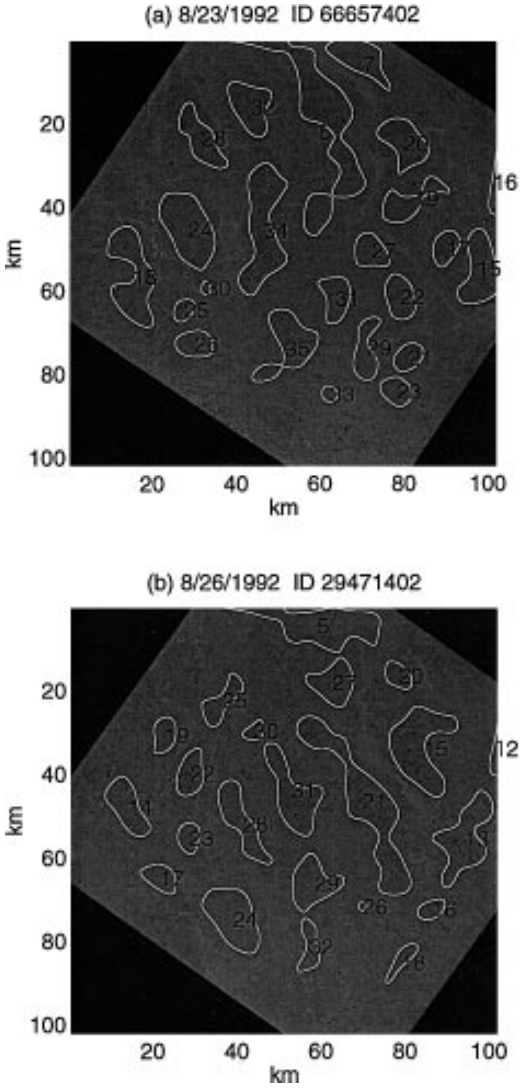

FIG. 10. Wavelet transform of SAR images in the Beaufort Sea with a medium scale from (a) 23 August and (b) 26 August 1992 with index for each closed contour.

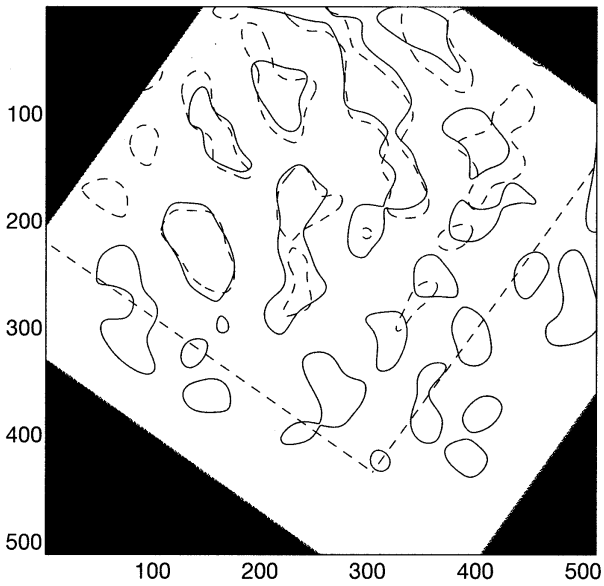

FIG. 11. Overlay of two contour maps from two different days in Fig. 10 by translation of a distance.

polynyas. For the summer case, the presence of liquid water on the ice surface greatly reduces the backscatter contribution from the sea ice. Due to the lack of features on the ice, this is one of the most difficult period for ice trackers. In spite of the lack of features, our multiscale wavelet analysis seems to work well in this case, and the detailed shape of ice floes are well delineated. Based on these detailed floe shapes, both the translation and rotation of the floes can be estimated from consecutive SAR images. In this technique, the wavelet analysis is concentrated on feature or pattern recognition and is fairly insensitive to the absolute calibration of the SAR data. The current method of template matching of ice floe shapes by use of a binary window obtained after manipulating the results of wavelet transform is very efficient computationally. This is mainly due to the fact that the only computation operations involved are bitwise logical operation and addition, while the classical template matching involves the operation of addition, square, and multiplication. Furthermore, it is only necessary to match the template pattern to a limited number of target patterns generated by the results of wavelet transform, not to every location in the images as with classical template matching.

In summary, the processing of SAR imagery with wavelet transforms is a rapid, efficient computational process. Therefore, the transforms can be used as a near-

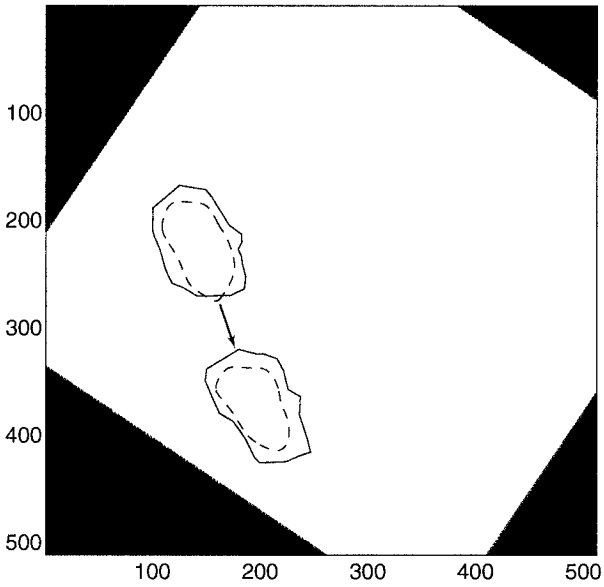

FIG. 12. Summary of the ice floe tracking results and the ice motion vector in the Beaufort Sea case.

real-time ''quick look'' for feature detection in SAR images, and the assimilation of SAR data with the mesoscale ocean–ice interaction model (Liu et al. 1993) can provide a cost-effective monitoring program to keep track of changes in important elements such as open leads, ice edges, and ice floes.

Acknowledgments. The authors thank Ben Holt for his valuable discussions and suggestions. We also gratefully acknowledge the role of the European Space Agency (ESA) and the Alaska SAR Facility in the generation and processing of these images. This work was supported by the National Aeronautics and Space Administration and the Office of Naval Research.

REFERENCES

Ballard, D. H., and C. M. Brown, 1982: *Computer Vision.* Prentice-Hall, 523 pp.

Canny, J., 1986: A computational approach to edge detection. *IEEE Trans. Pattern Analysis Machine Intelligence,* **8,** 679–698.

Cavalieri, D. J., and S. Martin, 1994: The contribution of Alaskan, Siberian, and Canadian coastal polynyas to the cold halocline layer of the Arctic Ocean. *J. Geophys. Res.,* **99,** 18 343–18 362.

Combes, J. M., A. Grossmann, and Ph. Tchamitchian, 1989: *Wavelet: Time Frequency Methods and Phase Space.* Springer-Verlag, 331 pp.

Kwok, R., J. C. Curlander, R. McConnell, and S. S. Pang, 1990: An ice-motion tracking system at the Alaska SAR Facility. *IEEE J. Oceanic Eng.,* **15,** 44–54.

Liu, A. K., and C. Y. Peng, 1993: Synthetic aperture radar for ocean applications. *Proc. Symp. on Remote Sensing in Environmental Research and Global Change,* Hong Kong, China, Hong Kong University of Science and Technology, 167–182.

——, S. Hakkinen, and C. Y. Peng, 1993: Wave effects on ocean–ice interaction in the marginal ice zone. *J. Geophys. Res.,* **98,** 10 025–10 036.

——, C. Y. Peng, and T. J. Weingartner, 1994: Ocean–ice interaction in the marginal ice zone using SAR. *J. Geophys. Res.,* **99,** 22 391–22 400.

McConnell, R. M., R. Kwok, J. C. Curlander, and S. S. Pang, 1991: Psi-s correlation and dynamic time warping: Two methods for tracking ice floes in SAR images. *IEEE Trans. Geosci. Remote Sens.,* **29,** 1004–1012.

Overland, J. E., and R. L. Colony, 1994: Geostrophic drag coefficients for the central Arctic derived from Soviet drifting station data. *Tellus,* **48A,** 75–85.

Schalkoff, R. J., 1992: *Pattern Recognition: Statistical, Structural, and Neural Approaches.* J. Wiley, 364 pp.

Thorndike, A. S., and R. L. Colony, 1982: Sea ice motion in response to geostrophic winds. *J. Geophys. Res.,* **87,** 5845–5852.